RSC Advances

PAPER

View Article Online
View Journal | View Issue

Cite this: *RSC Adv.*, 2023, **13**, 8753

Unveiling the effect of crystallinity and particle size of biogenic Ag/ZnO nanocomposites on the electrochemical sensing performance of carbaryl detection in agricultural products†

Nguyen Le Nhat Trang, [a] Dao Thi Nguyet Nga, [a] Lemma Teshome Tufa,[e] Van Tan Tran,[c] Thuan-Tran Hung,[d] Vu Ngoc Phan,[ac] Tuyet Nhung Pham, [a] Van-Tuan Hoang *[a] and Anh-Tuan Le *[ab]

In this study, bio-Ag/ZnO NCs were synthesized *via* a microwave-assisted biogenic electrochemical method using mangosteen (*Garcinia mangostana*) peel extract as a biogenic reducing agent for the reduction of Zn^{2+} and Ag^{+} ions to form hybrid nanoparticles. The as-synthesized NC samples at three different microwave irradiation temperatures (Z_{70}, Z_{80}, Z_{90}) exhibited a remarkable difference in size and crystallinity that directly impacted their electrocatalytic behaviors as well as electrochemical sensing performance. The obtained results indicate that the Z_{90} sample showed the highest electrochemical performance among the investigated samples, which is attributed to the improved particle size distribution and crystal microstructure that enhanced charge transfer and the electroactive surface area. Under the optimal conditions for carbaryl pesticide detection, the proposed nanosensor exhibited a high electrochemical sensitivity of up to 0.303 μA μM^{-1} cm^{-2} with a detection limit of LOD ~0.27 μM for carbaryl pesticide detection in a linear range of 0.25–100 μM. Overall, the present work suggests that bio-Ag/ZnO NCs are a potential candidate for the development of a high-performance electrochemical-based non-enzymatic nanosensor with rapid monitoring, cost-effectiveness, and eco-friendly to detect carbaryl pesticide residues in agricultural products.

Received 19th January 2023
Accepted 10th March 2023

DOI: 10.1039/d3ra00399j

rsc.li/rsc-advances

1. Introduction

Carbaryl (1-naphthyl methylcarbamate, $C_{12}H_{11}NO_2$) is the main ingredient in many commercial pesticides that have been widely used in agriculture to increase crop yield and enhance quality. However, their excessive residue products in soil, fruits, vegetables, and water can cause many negative effects on human health and the environment. Especially, they inhibit the catalytic activity of acetylcholinesterase (AChE) in the central nervous system and cause serious effects on humans and animals.[1,2] Because of the potential risks to people's health and animals, many countries have taken regulations on carbaryl limitation. For example, the carbaryl limit level in Europe is only in the concentration range from 0.01 mg kg^{-1} to 0.5 mg kg^{-1} for rice, fruits, and cereals. This allowable limit of Russia is from 0.02 mg kg^{-1} to 2.0 mg kg^{-1} in milk products, maize, and grains; and from 0.02 mg kg^{-1} to 25.0 mg kg^{-1} in olive oil.[3] Hence, it is necessary to develop a sensitive and robust method to determine carbaryl levels in foods.

Until now, many analytical methods have been developed for the detection of carbaryl in food, water, and drinks, including ultra-performance liquid chromatography with mass spectrometry (UPLC/MS),[4] reaction-resonance scattering spectroscopy, gas chromatography-mass spectrometry (GC-MS),[5] high-performance liquid chromatography (HPLC),[6] colorimetry,[7] fluorimetry,[8] surface-enhanced Raman spectroscopy,[9] and electrochemical methods.[10] Among them, the electrochemical sensor has received significant attention for the detection of carbaryl, due to their low expense, easy use, fast response, and high sensitivity. In addition, electrochemical sensors are also convenient for on-site determination and point-of-care testing.[11] For example, a novel electrochemical sensor based on graphene oxide-ionic liquid composite modified glassy carbon electrode (GCE) was used for the quick and ultra-

[a]*Phenikaa University Nano Institute (PHENA), Phenikaa University, Hanoi 12116, Vietnam. E-mail: tuan.hoangvan@phenikaa-uni.edu.vn; tuan.leanh@phenikaa-uni.edu.vn*

[b]*Faculty of Materials Science and Engineering (MSE), Phenikaa University, Hanoi 12116, Vietnam*

[c]*Faculty of Biotechnology, Chemical and Environmental Engineering (BCEE), Phenikaa University, Hanoi 12116, Viet Nam*

[d]*Center for Advanced Materials and Environmental Technology, National Center for Technological Progress, Hanoi 12116, Viet Nam*

[e]*Department of Chemical Engineering and Applied Chemistry, Chungnam National University, Daejeon, 34134, Republic of Korea*

† Electronic supplementary information (ESI) available. See DOI: https://doi.org/10.1039/d3ra00399j

sensitive detection of carbaryl with a detection limit (LOD) of 2 $\times 10^{-8}$ M.[12] Glass carbon electrode (GCE) was modified by a new polyaniline/CoAl-layered double hydroxide composite (PANI/CoAl-LDH) with the carbaryl detection limit of 6.8 $\times 10^{-9}$ M.[13] Reduced graphene oxide-wrapped silver nanoparticles (Ag@rGO) were utilized to modify the electrode surface with carbaryl being the detection target and the detection limit of 42 $\times 10^{-9}$ M.[14] Electrocatalysts of Pd and ZnO nanoparticles (NPs) supported on a highly porous framework of activated carbons (APC) were synthesized for electrochemical detection of carbaryl with a detection limit of 10^{-8} M.[15] Therefore, it is crucial to develop highly sensitive electrochemical sensors modified with eco-friendly materials to detect carbaryl.

Recently, the Ag/ZnO nanocomposites (Ag/ZnO NCs) were exposed as a candidate for the electrochemical nanosensor for organic agent trace detection.[16–18] Particularly, ZnO nanoparticles (NPs) possess a range of desirable traits, including wide availability, non-toxicity, robust mechanical strength, high thermal stability, antifouling and antibacterial properties, high specific surface area, efficient catalytic performance, and strong adsorption capabilities.[19,20] These properties make ZnO NPs an excellent choice for modifying working electrode surfaces in electrochemical sensors. However, ZnO NPs have poor charge transfer ability and rapid recombination of charge carriers, which are the main weak points of ZnO NPs for electrocatalysis applications.[21] To address these challenges, researchers have employed several approaches, including doping, modification, and hybridization, *etc.* As an effective way, ZnO NPs were combined with noble metal NPs to form metal–metal oxide interfaces.[22,23] The interesting studies of Ag/ZnO NCs have related to their morphology, size, component, and structure *via* some different synthesis methods, including bio-hydrothermal,[15,24] sol–gel method,[25] photo-chemical reduction,[26] chem-hydrothermal method,[27,28] and mechanochemical method.[29] Almost them displayed the impressive enhancements in electrochemical sensors toward toxic organic compounds. Using the one-pot hydrothermal method, an electrochemical sensor based on Ag/ZnO NCs was developed onto the ITO electrode, with a low limit detection of phosphorothioate pesticides of 0.010 μM. In addition, the photocatalytic performance of Ag/ZnO NCs was demonstrated for the degradation of Phox, with higher performance than pure ZnO nanorods. Therefore, modifying electrodes with Ag/ZnO NCs shows promising potential for the electrochemical sensor and photocatalytic degradation of toxic pesticides in the food and environmental fields.[30] N. Sebastian *et al.* have devoted to developing a sensitive electrochemical sensor based on silver-decorated zinc oxide (Ag/ZnO) material for the nanomolar-level detection of rhodamine B (RhB). The obtained result showed a low limit detection of 0.8 nM. Moreover, Ag/ZnO NCs was also found to be a remarkable photocatalyst for efficiently degrading RhB. The sensitive detection and degradation of dye are crucial to ensuring the safety of living being.[31] A novel biosensor was also successfully developed to detect xanthine in both meat and fish samples corresponding to limit detection of 0.07 μM. The electrode was covered with nano Ag–ZnO, which played an important role in the performance of the biosensor by significantly increasing the porous structure of the conducting polymer (pyrrole) surface.[32]

In this work, for the first time, we reported a green approach for the synthesis of Ag/ZnO NCs *via* a combined microwave-assisted/biogenic electrochemical method. Biomolecules from mangosteen peel extract not only played the role of biogenic reducing agent for the reduction of Zn^{2+} and Ag^{+} ions to form ZnO and Ag nanoparticles but also acted as stabilizers. The present work has exposed eco-friendly, easy-to-scale-up, and cost-effective methods. More interestingly, by tuning particle size distribution and crystal microstructure of Ag/ZnO NCs, their systematic impacts on electrocatalytic activity, conductivity, and sensing performance in electrochemical sensors based on biogenic Ag/ZnO NCs were clarified. Finally, according to the proposed approach, a rapid electrochemical-based non-enzymatic nanoplatform was proposed for carbaryl detection in agricultural products.

2. Experimental section

2.1. Chemicals and apparatus

Pure silver (Ag) bars were used as working electrodes in the electrochemical process, which were 10 and 15 cm high, 3 and 8 mm thick, respectively, and were purchased from a domestic jewellery company in Hanoi, Vietnam. Cabarryl (CBR, 98%), nitric acid (HNO_3, 63%), iron(III) nitrate ($Fe(NO_3)_3$, 99%), copper(II) sulfate ($CuSO_4$,99%), zinc nitrate ($Zn(NO_3)_2$, 99%), nickel(II) nitrate ($Ni(NO_3)_2$, 99%), potassium chloride (KCl, 99%), ascorbic acid ($C_6H_8O_6$, 99%), urea (CH_4N_2O, 99%) amoxicillin ($C_{16}H_{19}N_3O_5S$, 99%), and D-glucose ($C_6H_{12}O_6$, 99%) were purchased from Shanghai Chemical Reagent. Also, the double-distilled water used in the whole process was prepared using a Milli-Q® system (18.2 MΩ cm at 25 °C).

The phosphate-buffered saline (PBS) buffer solution (0.1 M, pH 7.2) was prepared by using NaCl, KCl, $Na_2HPO_4 \cdot 12H_2O$, and KH_2PO_4 (>99%, Merck KGaA, Germany). The pH of PBS buffer was adjusted by using H_3PO_4(0.1 M) and NaOH (2 M). All chemicals were used as received without any further purification. Carbon screen-printed electrodes (SPEs-DS110) were provided from DS Dropsens, Spain.

2.2. Synthesis of bio-Ag/ZnO NCs and bio-Ag/ZnO NCs-modified SPE

20 mL of plant extract, namely mangosteen (*Garcinia mangostana*) peel was added to a 200 mL beaker and stirred for 15 min. Two zinc (Zn) rods were placed 7 cm apart and dipped about 10 cm deep into the beaker used as the cathode and anode. A 20 V DC voltage source was applied to the electrodes. The electrochemical synthetic process was carried out for 2 h at room temperature without using any chemical additives. Similarly, the electrolysis process of the bare Ag rods was carried out. However, here the voltage supplied was about 10 V for 30 min. Next, the homogenized solution was subjected using UWave-2000 multifunctional microwave aiming to heating for 15 min with 250 W at different temperature conditions of 70 °C, 80 °C, and 90 °C, which were denoted as Z_{70}, Z_{80}, and Z_{90}, respectively.

All carbon screen-printed electrodes (SPEs) modified with bio-Ag/ZnO NCs were prepared by a simple dropping method. Briefly, all SPEs were washed several times with DI and ethanol, then dried at room temperature. Next, a solution of biological (bio-Ag/ZnO NCs) with various volumes from 4 to 12 μL was dripped onto the surface of the SPE working electrode and dried naturally in the air. The modified electrode was used for subsequent electrochemical experiments.

2.3. Preparation of real samples

Real samples were prepared from cabbage samples, which were purchased from the local supermarket. 3 g of the homogenized cabbage samples was carefully mixed with 10 mL of phosphate buffer (0.1 M) using a vortex mixer. Then, the obtained solution was sonicated for 30 min. The resulted solution was centrifuged for 5 min at 10 000 rpm and filtered through Whatman filter paper to get clear liquid phase. Finally, the known different amounts (10, 25, and 50 μM) of CBR standard were added to the obtained liquid phase.

2.4. Characterization techniques

The crystalline characterization and structural properties of bio-Ag/ZnO NCs were analyzed by a Bruker D5005 X-ray diffractometer (using Cu Kα radiation, $\lambda = 0.154056$ nm) under a voltage of 40 kV and a current of 30 mA. The absorption spectra of bio-Ag/ZnO NCs was measured by ultraviolet-visible (UV-vis) spectrophotometry (HP 8453 spectrophotometer). The morphology of bio-Ag/ZnO NCs was characterized by high-resolution transmission electron microscopy (HR-TEM, JEOL, JEM-3010, Tokyo, Japan). Particle size distribution was analyzed by dynamic light scattering (DLS) measurement (Horiba SZ-100). pH value was determined by an IC-PH60 pH tester kit. In addition, all electrochemical measurements were conducted on a three-electrode electrochemical cell (Palmsens4, PS Trace, PalmSens, The Netherlands) at room temperature.

2.5. Electrochemical measurements

The electrochemical properties of the bare electrode (bare SPE) and bio-Ag/ZnO NCs-modified electrodes were investigated *via* cyclic voltammetry (CV) and electrochemical impedance spectroscopy (EIS) techniques. CV measurements were carried out in 0.1 M KCl containing 5 mM $[Fe(CN)_6]^{3-/4-}$ as redox probes at a scan rate of 50 mV s^{-1} within the potential range from −0.3 V to 0.6 V. While, electrochemical impedance spectroscopy (EIS) was recorded in the frequency range of 0.01–50 kHz by applying an AC voltage of 10 mV amplitude. Electrolyte of 0.1 M phosphate buffer solution (PBS, pH 7.4) was prepared by dissolving 8 g NaCl, 0.2 g KCl, 1.44 g Na_2HPO_4, and 0.245 g KH_2PO_4 into 1000 mL DI water under the aid of magnetic stirring for 30 min at room temperature. The electrochemical behaviors of CBR on the modified electrodes were investigated using CV and differential pulse voltammetry (DPV) measurements in phosphate buffer (0.1 M PBS) containing different concentrations of CBR. The CV measurements were carried out in the potential range between 0 and 1.0 V, $T_{equilibrium} = 120$ s. The DPV measurements were completed as follows: scan rate of 6 mV s^{-1}, $T_{equilibrium} = 5$ s, $E_{pluse} = 0.05$ V, and $T_{pulse} = 0.2$ s in the potential range of 0.0 to 0.8 V.

3. Results and discussion

3.1. Characterization of bio-Ag/ZnO NCs

Bio-Ag/ZnO NCs were synthesized by a combined microwave-assisted/biogenic electrochemical method using mangosteen peel extracts. UV-vis spectroscopy and TEM were used to confirm the characteristic absorption peak and the morphology of bio-Ag/ZnO NCs (see Fig. 1). Fig. 1a shows the UV-vis spectra of the as-synthesized samples and the color of their solutions. After the electrochemical process, the color of the extracted mixture turned yellow-brown due to the formation of bio-Ag/ZnO NCs under microwave radiation. The UV-vis spectra of ZnO nanoparticles (NPs) showed a characteristic absorption peak centered at 334 nm, which is the characteristic peak for hexagonal wurtzite ZnO.[33] The formation of Ag NPs was confirmed by the characteristic surface plasmon resonance absorption band at 400–420 nm in the UV-vis region. As the increase in microwave temperature, the absorption peak intensity increased clearly meanwhile the absorption peak wavelength remained unchanged.

The morphology of bio-Ag/ZnO NCs could be viewed in Fig. 1b–d. It can be observed that NPs with different sizes were separately dispersed on the phytochemical matrix in the as-synthesized solution. The uniform near-spherical nanoparticle (average size of ∼20 nm) could correspond to Ag NPs. The others (average size of ∼50 nm) could correspond to bio-Ag/ZnO NCs due to Ag NPs decorated on ZnO NPs. The Z_{90} nanoparticles had small size, relatively uniform dispersion. However, Z_{70} and Z_{80} nanoparticles had large size, uneven distribution, and showed the phenomenon of agglomeration. The results of Fig. 1b'–d' show that the nanoparticle size distribution of the samples Z_{70}, Z_{80}, Z_{90} the range of 20 to 80 nm, 20 to 50 nm and 10 to 40 nm, respectively. The particle size distribution of these composite samples is further confirmed through the results of DLS spectroscopy (Fig. S1†). For more convincing evidence, the result of the HRTEM image analysis was shown in Fig. 2. Two different contrasting bands can be found within the boundary of bio-Ag/ZnO NCs. The 2.45 Å inter-plane distance corresponds to the (101) plane of ZnO, while the 2.02 Å inter-plane distance was assigned to the (200) lattice plane of Ag. The observed result confirmed that bio-Ag/ZnO NCs have formed in the as-synthesized sample.

Fig. 3 shows the crystallographic microstructure and particle size distribution of bio-Ag/ZnO NCs. As shown in Fig. 3, all three bio-Ag/ZnO NCs samples exhibited the appearance of characteristic peaks at 31.7°, 34.4°, 36.2°, 47.5°, and 56.6° that fix well with (100), (002), (101), (102), and (110) planes, respectively, of hexagonal wurtzite structure of ZnO (JCPDS standard card no. 36-1451). Furthermore, the other diffraction peaks were also observed at around 37.2°, 40.5°, 54.8°, and 76.1°, revealing the presence of Ag, according to JCPDS (87-0598) within the bio-Ag/ZnO NCs crystalline lattice structure. The average crystal size of ZnO NPs was calculated by the Debye–Scherrer equation, corresponding to 44 nm, 32 nm, and 23 nm for Z_{70}, Z_{80}, and Z_{90},

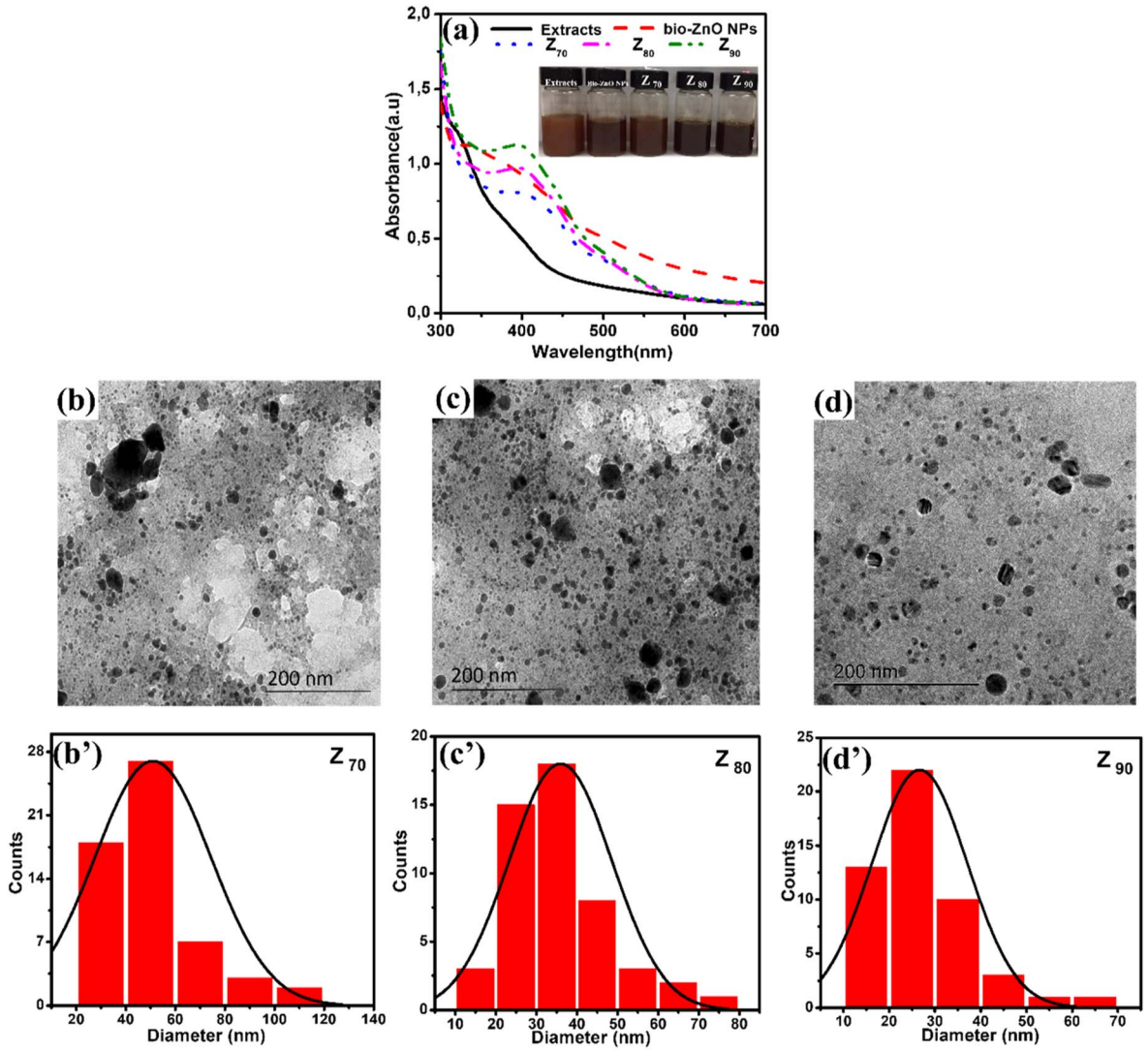

Fig. 1 (a) UV-vis spectra of the extract's samples, bio-ZnO NPs and Z_{70}; Z_{80}; Z_{90}. Inset pictures the glass vitals of the solutions, respectively; (b–d) the TEM images of Z_{70}; Z_{80}; Z_{90}; (b′–d′) histograms of the size distribution of Z_{70}; Z_{80}; Z_{90} samples, respectively.

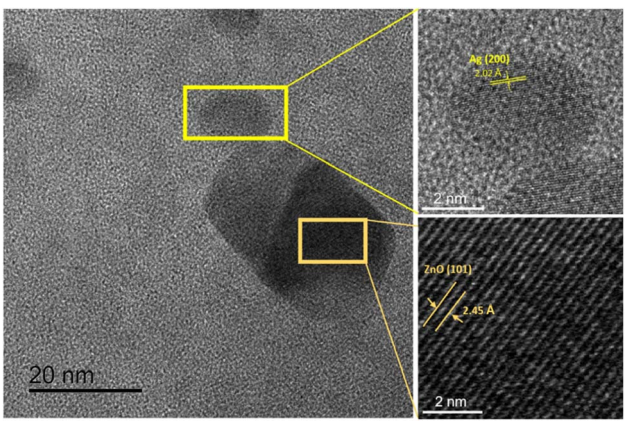

Fig. 2 The HRTEM images of Z_{90}.

respectively. For Ag NPs, the average crystal size of sample Z_{70} was estimated to be 25 nm, the values of Z_{80} and Z_{90} samples were 21 nm and 15 nm, respectively. The temperature favored the crystallization of bio-Ag/ZnO NCs nanocrystals. Obviously, increasing microwave temperature decreased the particle size. Smaller particles produced at higher temperatures could be attributed to the higher supersaturation ratio of metal atoms in the solution at faster temperature ramp rates.[34] Herein, the significant effect of the synthesis temperature on the size distribution was considered due to the impact of temperature on the motivation of ions within the solution. Indeed, at higher temperatures, the ions tend to move faster within the solution, leading to a low ability for collision and contact among ions. Thus, it reduces and inhibits the crystallization ability as well as the formation of particle size.[35,36] Clearly, Z_{90} showed more unique features in not only size and crystallinity. Thus, Z_{90} was expected as a key candidate possessing a high potential for electrocatalytic activity and electron conductivity in the sensing

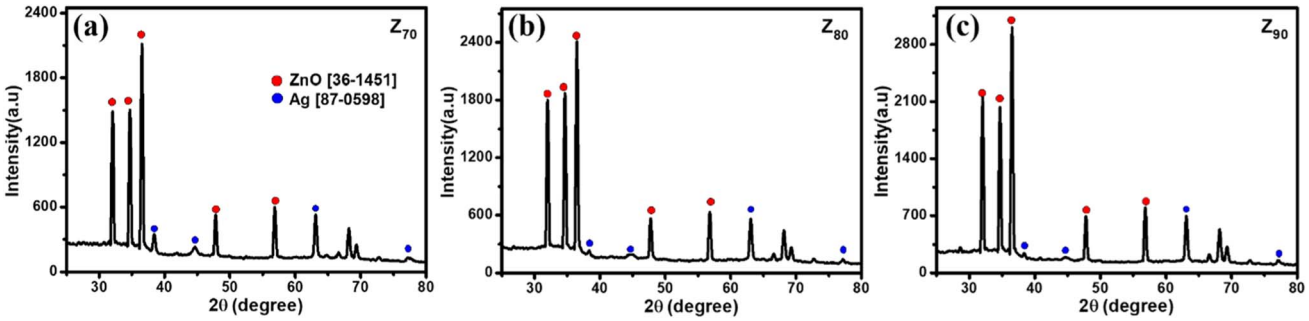

Fig. 3 (a); (b); (c) XRD spectrum of Z_{70}; Z_{80}; Z_{90}, respectively.

electrode. Crystal structure and particle size distribution were the factors that were reported a decisive influence on their electrocatalytic activity, conductivity, and electrochemical sensing performance.[37–39] This relationship was further studied and discussed in more detail in the following sections.

3.2. Electrochemical characteristics of the modified electrodes

The electrochemical properties of the modified electrodes were investigated by CV and EIS measurements using a standard redox probe, $[Fe(CN)_6]^{3-/4-}$, aiming to explore the role of the crystal structure of bio-Ag/ZnO NCs on CBR electrochemical sensing performance. Fig. 4a shows the CV curves of bare SPE and modified electrodes (Z_{70}/SPE, Z_{80}/SPE, and Z_{90}/SPE) in 0.1 M KCl containing 5 mM $[Fe(CN)_6]^{3-/4-}$ at a scan rate of 60 mV s^{-1}. The obtained CV curves exhibited a pair of oxidations–reduction peaks, corresponding to the electron transfer of Fe^{2+} reversibly into Fe^{3+}. Notably, all the modified electrodes showed a remarkable enhancement in current response, compared to bare SPE. Indeed, the reduction peak currents were about 58.16 μA, 90.15 μA, 117.24 μA, and 151.2 μA for bare SPE, Z_{70}/SPE, Z_{80}/SPE, and Z_{90}/SPE, respectively. Modified electrodes clearly exhibited higher electrochemical properties than the bare electrode. Among them, Z_{90}/SPE had the highest reduction/oxidation current response, suggesting that crystal structure and particle size distribution of bio-Ag/ZnO NCs have a strong influence on the resistivity of the modified electrodes. Accordingly, the obtained results reveal that Z_{90}/SPE promises a better electrochemical sensing performance than others.

To investigate the charge transfer capacity of the variable electrodes, electrochemical impedance spectroscopy (EIS) measurements were performed. Nyquist plots of Z_{70}/SPE, Z_{80}/SPE, and Z_{90}/SPE in 0.1 M KCl containing 5 mM $[Fe(CN)_6]^{3-/4-}$ in the frequency range 50 kHz–0.01 Hz with amplitude 10 mV of a.c. voltage have been shown in Fig. 4b. For all electrodes, for the EIS measurements, the R_{ct} values of SPE, Z_{70}/SPE, Z_{80}/SPE, and Z_{90}/SPE were calculated of (731 ± 1.0) Ω, (620 ± 0.71) Ω, (473 ± 0.81) Ω, and (347 ± 0.9) Ω, respectively. Obviously, there is a notable decrease in R_{ct} in modified electrodes with the smallest R_{ct} of Z_{90}/SPE. The decrease in R_{ct} of smaller samples could be attributed to both higher volume fractions of smaller NPs packed inside the film and higher crystallinity which facilitated the charge transfer.

Fig. 5a–d shows CV curves recorded at bare SPE and modified electrodes in 0.1 M KCl containing 5 mM $[Fe(CN)_6]^{3-/4-}$

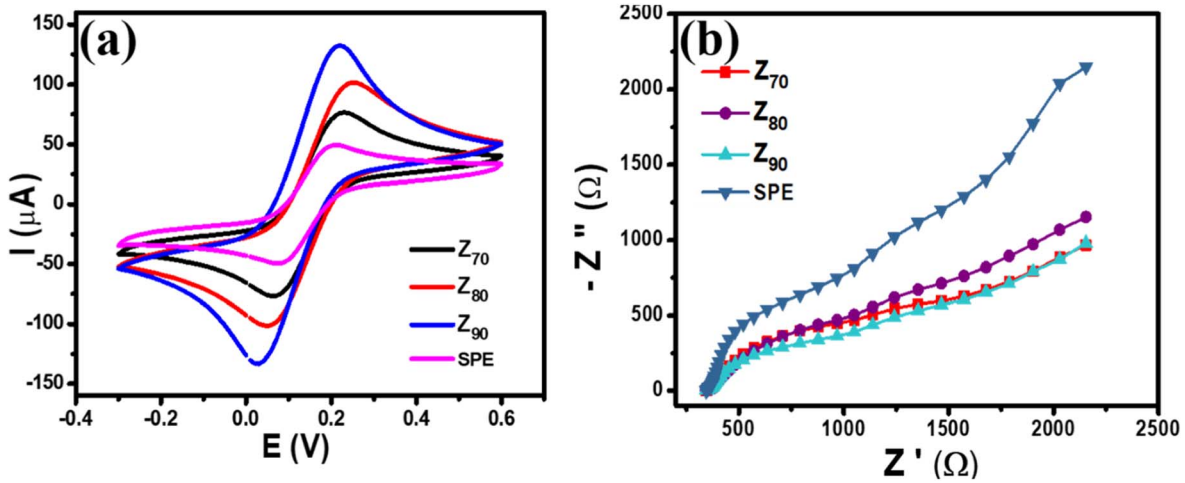

Fig. 4 (a) CV profiles of various modified electrodes at scan rate 60 mV s^{-1} in 0.1 M KCl containing 5 mM $[Fe(CN)_6]^{3-/4-}$ (b) EIS profiles of various modified electrodes.

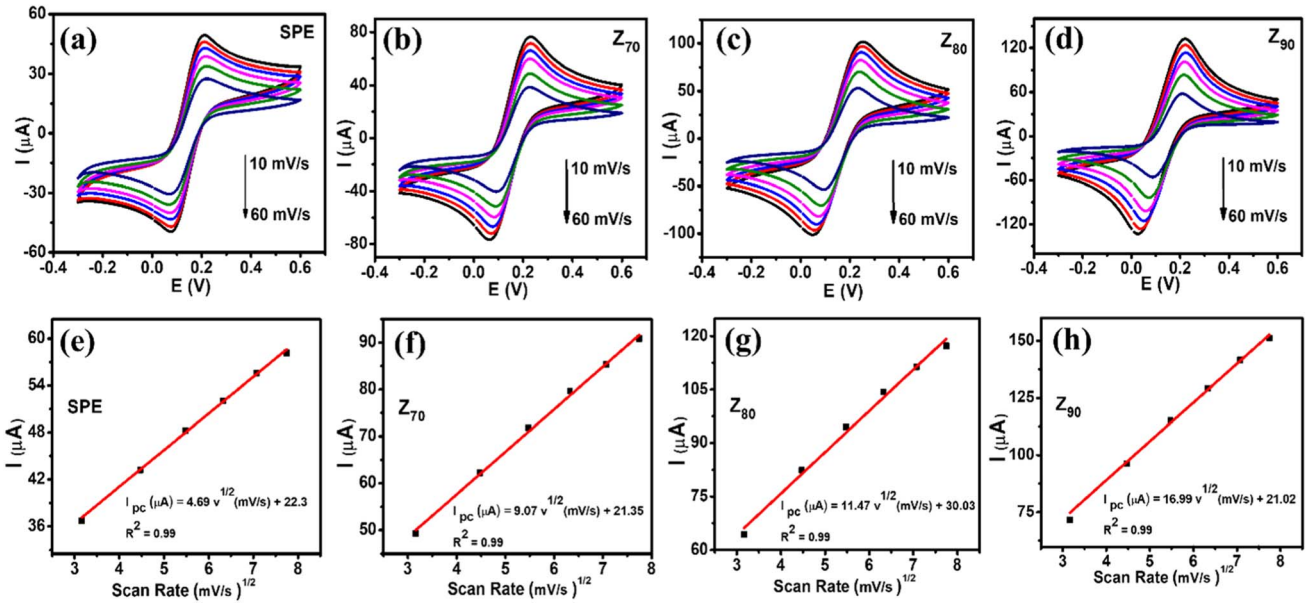

Fig. 5 (a–d): CV profiles of modified electrodes at various scan rates (10–60 mV s^{-1}); and (e–h): the corresponding linear plot of reduction peak current response and sqrt of scan rate. All experiments were performed in 0.1 M KCl containing 5 mM $[Fe(CN)_6]^{3-/4-}$.

with various scan rates from 10 to 60 mV s^{-1}. It can be seen that the observed peak current increased with an increase in scan rate from 10 to 60 mV s^{-1}. Their corresponding linear plots of current response (I, which is the average of three consecutive measurements I_1, I_2, I_3 of the amperage value: $I = (I_1 + I_2 + I_3)/3$) against the square root of scan rate were presented in Fig. 5e–h, suggesting the redox reaction onto all the electrode surfaces was a diffusion-controlled process.[37,40] To further explain the enhancement of the current intensity, the electroactive surface area (EASA) value, which reflects the total electrochemically active area, was calculated based on the Randles–Sevick equation:

$$I_p = 2.69 \times 10^5 A n^{3/2} D^{1/2} C \nu^{1/2} \quad (1)$$

where I_p presents the cathodic and anodic peak current, n is the number of electron transfer, D is diffusion coefficient of $[Fe(CN)_6]^{3-/4-}$, A is electroactive surface area (EASA), ν is the potential scan rate, and C is the concentration of $[Fe(CN)_6]^{3-/4-}$. Herein, EASA was estimated from the graphs of cathodic peak current along with $n = 1$, $D = 6.5 \times 10^{-6}$ cm s^{-1}, $C =$ 5 mM, and $\nu = 0.05$ V s^{-1}. The calculation results indicate that the active surface area of the electrode was improved by the addition of bio-Ag/ZnO NCs. In which, the EASA value of Z_{90}/SPE was the highest (0.495 cm^2) and 3.6-fold larger than that of bare SPE (0.137 cm^2). The EASA values of Z_{80}/SPE (0.335 cm^2) and Z_{70}/SPE (0.265 cm^2) were also 2.5-fold and 1.9-fold higher than those of bare SPE, respectively. This result could be due to the difference in distribution size and crystallinity of bio-Ag/ZnO NCs, leading to get a larger active surface area. The CV and EIS results indicate that Z_{90}/SPE also exhibited the best electrochemical performance among the investigated modified electrodes.

3.3. Electrochemical sensing performance of the modified electrodes

The electrochemical behavior of CBR at bio-ZnO NPs, bio-AgNPs, bio-Ag/ZnO, and Z_{70}-modified electrodes in PBS buffer solution (pH 3) was considered by typical CV at a scan rate of 50 mV s^{-1} (Fig. 6a). It can be seen that the strongly increased oxidation peak occurs at 0.58 V for the SPE, 0.55 V for the three electrodes modified with bio-ZnO NPs, bio-Ag/ZnO, and Z_{70}, particularly the lowest potential at 0.46 V for the electrode modified with bio-AgNPs. This peak could be assigned to the carbaryl oxidation which is consistent with some previous reports regarding the oxidation peak of CBR.[12,41] Fig. 6b shows a bar plot of the irreversible oxidation peak current response for CBR for all modified electrodes. Indeed, the oxidation peak current response of CBR at bio-ZnO NPs (3.82 μA), bio-AgNPs (4.64 μA), bio-Ag/ZnO (5.52 μA), and Z_{70} (6.73 μA) was 1.1-fold, 1.4-fold, 1.7-fold and 2.0-fold higher as compared with bare SPE (3.34 μA), respectively. Among them, Z_{70} offered the highest anodic peak current compared with other modified electrodes. It is clear that the Z_{70} sample with microwave assistance enhanced significantly the amperage signal compared with the rest of the samples. Therefore, the Z_{70} sample was selected to conduct further experiments.

To evaluate the electrochemical activity of different electrodes, the CV response of SPE and SPE modified with Z_{70}/SPE, Z_{80}/SPE, and Z_{90}/SPE were measured in PBS buffer solution (pH 3.0) at a scan rate of 50 mV s^{-1}. Fig. 6c shows the CV curves of all four electrodes in 0.1 M PBS (pH 3) containing 100 μM CBR. It can be seen that a sharp increase in oxidation peak occurred at 0.58 V, 0.55 V, 0.53 V, and 0.5 V for SPE, Z_{70}/SPE, Z_{80}/SPE, and Z_{90}/SPE, respectively. For modified electrodes, the sharp oxidation peaks were recorded as the oxidation process of CBR at the potential. It is found that the oxidation peak potential on

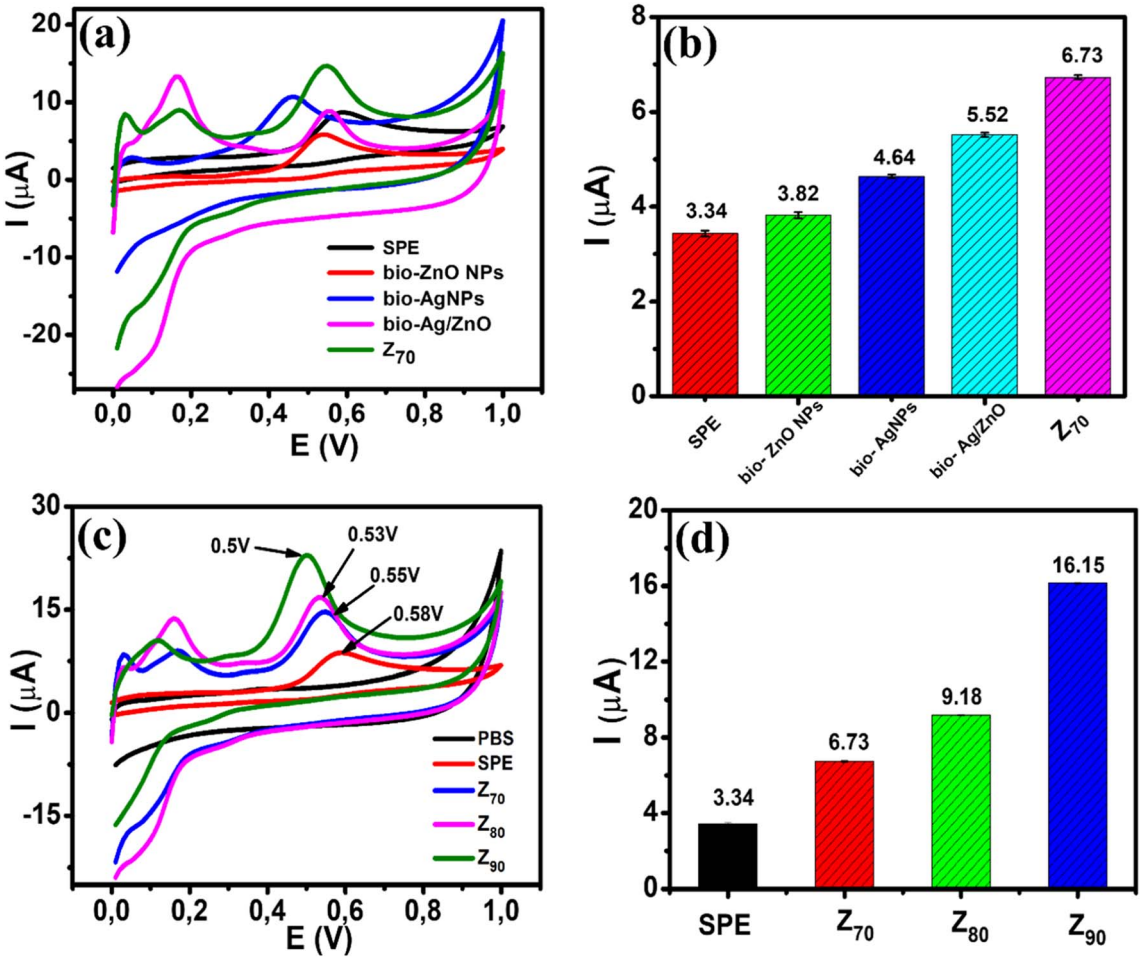

Fig. 6 (a) CV curves of bio-ZnO NPs, bio-AgNPs, bio-Ag/ZnO, Z_{70} modified electrodes using 0.1 M PBS (pH 3.0) in 100 mM CBR; (b and d) the corresponding bar chart diagram of irreversible oxidation peak current responses for CBR; (c) CV curves of SPE and Z_{70}/SPE, Z_{80}/SPE, and Z_{90}/SPE-modified electrodes using 0.1 M PBS (pH 3.0) in 100 μM CBR. The scan rate is 50 mV s^{-1}.

Z_{90} shifted to a more positive direction, compared to Z_{70} and Z_{80}, consuming less energy required for the electrochemical oxidation of CBR. The difference in oxidation peak potential may be due to the change in crystallinity. Fig. 6d shows a bar chart diagram of irreversible oxidation peak current responses towards CBR for all three modified electrodes. Compared to the bare SPE, all the modified SPEs showed an increase in the oxidation peak current, indicating that the bio-nanocomposites significantly improved the electrochemical activity for CBR oxidation. Among them, Z_{90} offered the highest anodic peak current of about 16.15 μA, which is ~1.8 times higher than Z_{80} (9.18 μA), 2.4 times higher than Z_{70} (6.73 μA), and 4.8 times higher than bare electrode (3.34 μA). It is clear that the size and crystallinity of Ag/ZnO NCs were important factors, affecting the electrochemical sensing performance for detecting CBR.

3.4. The effect of scan rate and pH

The influence of experimental parameters, including pH value, scanning speed, accumulation time, and electrode coating volume on the sensing performance were investigated and optimized. To understand the mechanism of electron transfer reaction occurring onto the modified electrode surface, the effect of scanning speed and pH value on the oxidation potential as well as the current response of CBR were investigated by CV measurements. Based on relationship between sweep rate and peak amperage or voltage response, kinetic studies calculated from CV measurements were performed. Fig. S2† illustrates the effect of different sweep rates (10–60 mV s^{-1}) on the electrochemical behaviors of CBR in 0.1 M PBS (pH 3) containing 100 μM CBR for modified electrodes. Apparently, the increases in both anode and cathode peak currents were observed along with the increase in the scan rate for the investigated electrodes. Calibration graphs between CBR irreversible peak oxidation current and sweep rate were described with linear regression equations:

$$Z_{70}: I_p\ (\mu A) = 0.14v\ (\text{mV s}^{-1}) + 0.137;\ R^2 = 0.99$$

$$Z_{80}: I_p\ (\mu A) = 0.18v\ (\text{mV s}^{-1}) + 0.194;\ R^2 = 0.99$$

$$Z_{90}: I_p\ (\mu A) = 0.29v\ (\text{mV s}^{-1}) + 2.06;\ R^2 = 0.99$$

Accordingly, CBR oxidation was a typical surface adsorption-controlled process rather than a diffusion process. More interestingly, the adsorption capacity of CBR on the electrode surface of Z_{90}/SPE was also determined through the equation:[42,43]

$$I_p = n^2F^2Av\Gamma/4RT \quad (2)$$

With the observed slope values, the adsorption capacity (Γ) of Z_{70}/SPE, Z_{80}/SPE, and Z_{90}/SPE were approximately 4.5×10^{-7} mol cm^{-2}, 5.9×10^{-7} mol cm^{-2}, and 9.3×10^{-7} mol cm^{-2}. Therefore, the Z_{90}-modified electrode exhibited the largest adsorption capacity. At the same time, the small change in the CBR peak potential was observed with an increasing sweep rate. Indeed, the anodic peak potential of CBR shifted in the positive direction according to a linear relationship with ln(v), corresponding to the regression equations respectively:

$$Z_{70}\text{: } E_{pa} = 0.029 \ln v \text{ (V s}^{-1}\text{)} + 0.634 \ (R^2 = 0.99)$$

$$Z_{80}\text{: } E_{pa} = 0.031 \ln v \text{ (V s}^{-1}\text{)} + 0.627 \ (R^2 = 0.99)$$

$$Z_{90}\text{: } E_{pa} = 0.033 \ln v \text{ (V s}^{-1}\text{)} + 0.608 \ (R^2 = 0.99)$$

Based on the Laviron equation:[44,45]

$$E_{pa} = E^0 + ((RT/(1-\alpha)nF) \times \ln((1-\alpha)nF)/RTk_{et}) + (RT/(1-\alpha)nF)\ln(v) \quad (3)$$

According to that, the slope of a straight–line plot yielded by $E = f(\ln v)$ equaled to $RT/((1-\alpha)nF)$, where R is the gas constant ($R = 8.314$ J mol^{-1} K^{-1}), $T = 300$ K, a is the electron transfer coefficient, F is the Faraday constant ($F = 96\,485.33$ C mol^{-1}), n is the number of electrons transferred, and k_{et} is the electron transfer rate constant. From the determined slope values, the number of transfer electrons (n) in the electron transfer reaction could be determined to be 1 for CBR, corresponding to the charge transfer coefficient (α) found of 0.1, 0.16, and 0.21 for Z_{70}/SPE, Z_{80}/SPE, and Z_{90}/SPE, respectively. More importantly, the electron transfer rate constant (k_{et}) was calculated approximately 1.56 s^{-1} for Z_{90}, 0.74 s^{-1} for Z_{80}, and 0.34 s^{-1} for Z_{70}. As we know, the electron transfer number in the redox reaction directly affects the current intensity and they are usually proportional to each other.[42] Thus, Z_{90} exhibited the largest electron transfer rate constant (k_{et}), demonstrating high electron conduction and faster response than the other electrodes.

The impact of pH on the amperage and oxidative peak potential of CBR for bio-Ag/ZnO NCs was investigated by the DPV technique. The DPV curve of Z_{90} for 100 μM CBR in 0.1 M PBS with different pHs between pH 2 and pH 7 was shown in Fig. S3.† Obviously, the peak current response of CBR increased gradually as the pH varies from 2 to 3. However, beyond a pH value of 3, a further increase in pH led to a decrease in the peak current response. Obviously, at a pH value of 3, the CBR oxidation reaction reached a maximum. The obtained results could be explained by the fact that at low pH, the naphthol molecules can be protonated. This caused the diminution of peak current and affected the oxidation process. These results are similar to some previous reports.[11] Therefore, pH 3 was chosen for CBR detection, which is consistent with some previous publications.[46]

Furthermore, with increasing solution pH, the peak potential turned negative, which infers that the oxidation of CBR involves protons. According to the regression equation of $E = -0.0393$ pH + 0.547 ($R^2 = 0.99$) in Fig. S2b,† the slope value of -0.0393 V pH^{-1} was the same as the theoretical value of Nernst $-(m*0.59)/n$ (V pH^{-1}), where m and n represent the number of protons and electrons transferred. As a result, one proton and electron were involved in the electrochemical oxidation that occurred at the electrode surface. The Z_{90}-modified SPE electrode was investigated from 30 to 150 s to determine the optimal accumulation time. The results are shown in Fig. S4.† The peak amperage (I_p) obviously increased with increasing accumulation time and peaked at 120 s. Therefore, the accumulation time was optimized to be 120 s for the subsequent experiments.

To optimize the Z_{90} coating volume on SPE, the electrochemical response of Z_{90}/SPE with different dropping volumes from 4 to 12 μL was investigated by DPV technique towards 100 μM CBR detecting in 0.1 M PBS at a high sweep rate 60 mV s^{-1} (Fig. S5†). The oxidation peak current increased significantly with increasing coating volume from 4 to 8 μL. After that, the peak current gradually decreased as the adjusted coating volume increased. It is possible that when the increased volume caused the formation of thick layers of material on the electrode surface, this not only hindered the electron transfer within the electrode and the access of the electrolyte to the electrode surface but also led to easy peeling, breaking the working electrode during operation. Therefore, the optimal value of Z_{90} volume was suggested to be 8 μL for subsequent electrochemical measurements.

3.5. Effect of crystallinity and size distribution of bio-Ag/ZnO NCs on electrochemical sensing performance

The DPV technique was used to evaluate the CBR sensing performance of various biological AgNPs-based electrochemical sensors. Fig. 7 shows the DPV curves of CBR with different concentrations on electrodes modified with Z_{70}/SPE (a), Z_{80}/SPE (b), and Z_{90}/SPE (c) in 0.1 M PBS (pH 3), suboptimal conditions, and calibration graphs of peak amperage, corresponding to different concentrations of CBR. It is clear that the amperage increased as the CBR concentration increased for all samples. Calibration plots were constructed for each modified electrode with a correlation coefficient R^2 greater than 0.99, as shown in Fig. 7d–f. The regression equation was found to be I_p (μA) = 0.056C (μM) + 0.03 ($R^2 = 0.99$) for Z_{70}/SPE in the CBR concentration range of 1–100 μM. For sample Z_{80}: I_p (μA) = 0.058C (μM) + 0.05 ($R^2 = 0.99$) in CBR concentration range from 10–100 μM and I_p (μA) = 0.11C (μM) + 0.013 ($R^2 = 0.99$) in the shorter CBR concentration range of 0.5–10 μM. And I_p (μA) = 0.08C (μM) + 0.106 ($R^2 = 0.99$) in the CBR concentration range of 25–100 μM and I_p (μA) = 0.12C (μM) + 0.07 ($R^2 = 0.99$) in the CBR concentration range from 0.25–25 μM for Z_{90}/SPE. Furthermore, it was observed that the oxidation potential slightly shifted to a more negative direction with increasing CBR concentration,

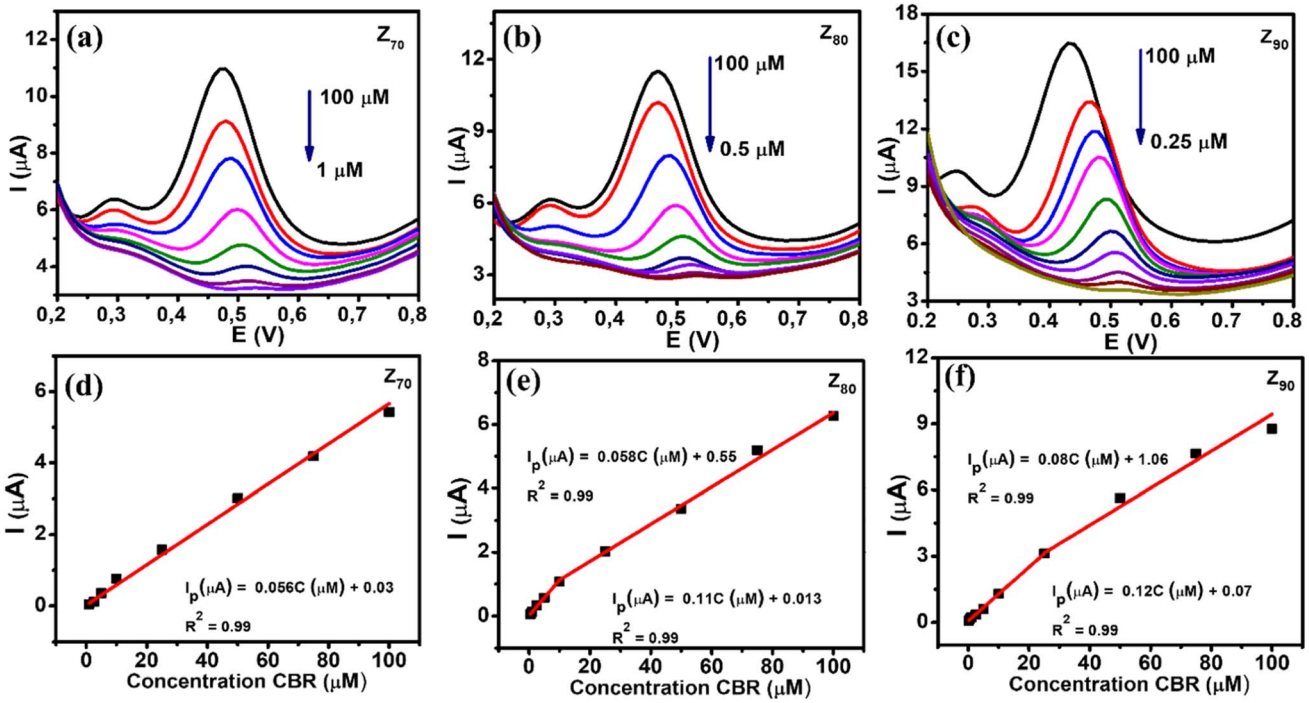

Fig. 7 DPV curves of various concentrations of CBR in 0.1 M PBS (pH 3) at scan rate 50 mV s^{-1} of Z_{70}/SPE (a), Z_{80}/SPE (b), and Z_{90}/SPE (c), corresponding to the calibration plots of peak current intensity *vs.* various concentrations of CBR (d–f) with error bar.

which was attributed to proton involvement and the change in pH value around the electrode surface.

Compared to the other samples, the Z_{90} exhibited the highest electrochemical sensitivity up to 0.303 μA μM^{-1} cm^{-2} with a CBR lowest detection limit of about 0.27 μM over a wider linear range (0.25–100 μM). The electrochemical sensitivity of Z_{80} was calculated as 0.27 μA μM^{-1} cm^{-2} with a detection limit of about 0.34 μM with a linear range of 0.5–100 μM. While sample Z_{70} the lowest electrochemical sensitivity of about 0.21 μA μM^{-1} cm^{-2} with detection limit of 0.64 μM, linear range 1–100 μM. In summary, Z_{90} achieved a higher sensitivity with lower LOD over a wider linear range for CBR detection than Z_{70} and Z_{80}.

The difference in size, crystallinity, and distribution are important parameters that decisively influence the conductivity, electrocatalytic activity, and adsorption efficiency of the transformed electrodes change. The order of grain size is $Z_{90} < Z_{80} < Z_{70}$, respectively, and crystallinity increases with increasing microwave temperature. Besides, the EASA value and R_{ct} value were recorded in the order $Z_{70} < Z_{80} < Z_{90}$ and $Z_{90} < Z_{80} < Z_{70}$. The higher the temperature, the smaller the particle size, and the greater the crystallinity. In general, the smaller particle size is the origin of the larger electroactive surface area and is vital for enhancing electrochemical performance. There have been a number of publications indicating that the electrocatalytic properties increase with decreasing size and crystallinity of nanoparticles.[37,47,48] Such potential characteristics have contributed to the enhancement of EASA value, electronic conductivity, and electrochemical response for CBR electrochemical detection. These results emphasize the synergistic effects of size, crystallinity, and distribution on electrochemical sensing performance.

The oxidation of CBR in the presence of Ag/ZnO NCs was proposed by two processes as follows:[11,49,50]

(1) In alkaline media with adding of NaOH, CBR molecules were hydrolyzed to 1-naphthol.

(2) Then, the [OH^-] functional group within 1-naphthol was oxidized with removing of 1 electron and 1H^+, corresponding to the appearance of a well-defined oxidation peak at 0.5 V.

The electrochemical mechanism of CBR was displayed as Fig. 8.

3.6. Repeatability, stability, reproducibility, and selectivity studies of the electrochemical sensing system

Under the optimal conditions, the repeatability of the modified electrodes was evaluated by recording the current response in the presence of 100 μM CBR for 10 consecutive times on the same electrode (Fig. S6†). The obtained results demonstrate that this sensor has good repeatability with relatively low standard deviation (RSD) values of 1.14%, 1.03%, and 1.02% for Z_{70}/SPE, Z_{80}/SPE, and Z_{90}/SPE, respectively. The selectivity of this modified electrode was analyzed by the DPV technique in the presence of several different interfering compounds and ions. The test results were shown in Fig. S7.† The obtained results showed the presence of 200 μM of some ions (Ni^{2+}, Fe^{2+}, Cu^{2+}, NO_3^-, and SO_4^{2-}) and 200 μM of compounds such as D-glucose, ascorbic acid, urea, thiram, amoxicillin, chloramphenicol, and furazolidone did not interfere in the determination of CBR. To evaluate the practical applicability of an electrochemical sensor based on bio-nanocomposites in a real sample, cabbage

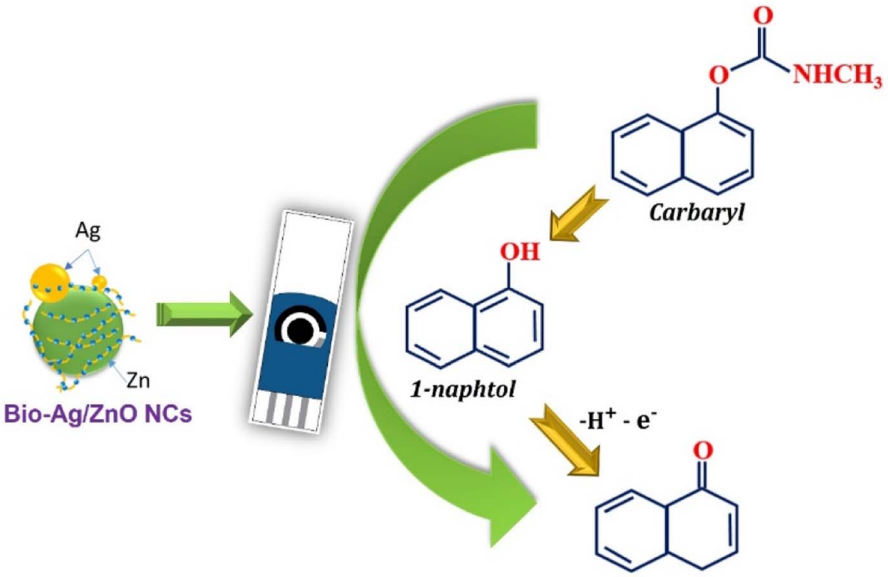

Fig. 8 Schematic illustration of the enhanced mechanism of electrochemical sensing performance of CBR using SPE electrode modified.

Table 1 Determination results of CBR in cabbage samples ($n = 3$)

Electrode	Amount added (μM)	Amount found (μM)	Recovery (%)	RSD (%)
Z_{70}/SPE	10	48.46	96.93	2.27
	25	22.61	90.45	1.22
	50	9.31	93.10	1.69
Z_{80}/SPE	10	46.72	93.45	1.41
	25	24.75	98.99	1.58
	50	9.64	96.39	2.15
Z_{90}/SPE	10	49.16	98.33	1.35
	25	23.99	95.98	0.93
	50	9.33	93.33	2.22

samples with adding CBR were used. Different concentrations of CBR of 10 μM, 25 μM, and 50 μM were spiked into cabbage samples and then analyzed by the DPV technique. The final concentration of CBR was calculated according to the regression equation of the calibration curves, as summarized in Table 1. The mean recoveries for Z70 were found to range from 91% to 97% with deviations. The relative standard (RSD) was within 1.2–2.3% ($n = 3$). Z_{80}/SPE, and Z_{90}/SPE show average recovery between 93% and 98% and RSD around 2.2%. The calculation results also demonstrate that the modification with this composite nanomaterial can be used effectively to control and monitor CBR in cabbage samples.

4. Conclusions

In summary, bio-Ag/ZnO NCs were successfully synthesized using a combined microwave-assisted/biogenic electrochemical method with mangosteen (*Garcinia mangostana*) peel extract. The obtained results show that microwave temperature impacted the characterization of as-synthesized samples. The relationship between tuning particle size distribution and crystal structure of bio-Ag/ZnO NCs on the electrochemical response of nanosensors was considered. It found that Z_{90}/SPE exhibited the best electrochemical performance among the investigated modified electrodes. This provides an insight that enhanced electrochemical activity can be achieved by controlling the crystallinity as well as the particle size distribution of their nanomaterial-assembled layer on the electrode. For carbaryl detection, the Z_{90}/SPE exhibited the highest sensing performance, good reproducibility, and reliability with electrochemical sensitivity up to 0.303 μA μM^{-1} cm^{-2} with a detection limit of ~0.27 μM in wider linear range (0.25–100 μM). The proposed electrochemical-based non-enzymatic sensor can reliably detect carbaryl in cabbage samples with an average recovery of 98%. The present study revealed that bio-Ag/ZnO NCs offered great promise for designing a high-performance electrochemical-based non-enzymatic nanosensor.

Author contributions

N. L. N. Trang: conceptualization, formal analysis, writing-original draft; D. T. N. Nga: formal analysis, writing-original draft; T. H. Thuan: methodology, formal analysis; L. T. Tufa: methodology, formal analysis; T. V. Tan: methodology, validation formal analysis, writing-review & editing; V. N. Phan: methodology, formal analysis; P. T. Nhung: investigation, formal analysis, writing-review & editing; H. V. Tuan: funding acquisition, formal analysis, writing-review & editing; L. A. Tuan: conceptualization, methodology, project administration, writing-review & editing.

Conflicts of interest

The authors declare that they have no known competing financial interests or personal relationships that could have appeared to influence the work reported in this paper.

Acknowledgements

This research was supported by Phenikaa University under grant number 2-04.2021.03. The authors would like to acknowledge the support for Raman, Electrochemical & UV-vis measurements from NEB Lab (Phenikaa University) and Zeta potential, DLS measurements from DKSH Lab at the Phenikaa University.

References

1 R. Krieger and W. Krieger, *Index*, Academic Press, San Diego, 2nd edn, 2001, pp. 1897–1908, DOI: 10.1016/B978-012426260-7/50092-6.
2 R. Gupta, *Index*, Academic Press, Burlington, 2006, pp. 735–763. DOI: 10.1016/B978-012088523-7/50051-X.
3 *The WHO Recommended Classification of Pesticides by Hazard*, 2019.
4 N. Abdullah, J. Zaidan, Z. A. Alothman, S. M. Wabaidur, A. A. Ghafar and T. Saleh, Journal of King Saud University – Science Development of a sensitive liquid-liquid extraction and ultra-performance liquid chromatography-tandem mass spectrometry method for the analysis of carbaryl residues in fresh vegetables sold in Riyadh, *J. King Saud Univ., Sci.*, 2020, 4, DOI: 10.1016/j.jksus.2020.03.030.
5 K. Elmamoun, A. Ibrahim and D. Şolpan, Removal of carbaryl pesticide in aqueous solution by UV and UV/hydrogen peroxide processes, *Int. J. Environ. Anal. Chem.*, 2020, 1–15, DOI: 10.1080/03067319.2020.1767091.
6 X. Song, Y. Shi and J. Chen, Carbon nanotubes-reinforced hollow fibre solid-phase microextraction coupled with high performance liquid chromatography for the determination of carbamate pesticides in apples, *Food Chem.*, 2013, **139**, 246–252, DOI: 10.1016/j.foodchem.2013.01.112.
7 X. Jing, H. Wang, X. Huang, Z. Chen, J. Zhu and X. Wang, Digital image colorimetry detection of carbaryl in food samples based on liquid phase microextraction coupled with a microfluidic thread-based analytical device, *Food Chem.*, 2021, **337**(2020), 127971, DOI: 10.1016/j.foodchem.2020.127971.
8 A. Ratiometric, *A Ratiometric Fluorescence Nanoprobe Using CdTe QDs for Fast Detection of Carbaryl Insecticide in Apple*, Talanta, 2020, p. 121467, DOI: 10.1016/j.talanta.2020.121467.
9 Y. Fan, K. Lai, B. A. Rasco and Y. Huang, LWT – Food Science and Technology Determination of carbaryl pesticide in Fuji apples using surface-enhanced Raman spectroscopy coupled with multivariate analysis, *LWT–Food Sci. Technol.*, 2015, **60**(1), 352–357, DOI: 10.1016/j.lwt.2014.08.011.
10 T. Rahmani and H. Bagheri, Modified 3D Graphene-Au as a Novel Sensing Layer for Direct and Sensitive Electrochemical Determination of Carbaryl Pesticide in Fruit, Vegetable and Water Samples, *Food Anal. Methods*, 2018, 3005–3014.
11 F. E. Salih, *et al.*, Electrochemical Sensor Based On Low Silica X Zeolite Modified Carbon Paste For Carbaryl Determination, *J. Adv. Res.*, 2017, **8**, 669–676, DOI: 10.1016/j.jare.2017.08.002.
12 B. Liu, B. Xiao and L. Cui, Journal of Food Composition and Analysis Electrochemical analysis of carbaryl in fruit samples on graphene oxide-ionic liquid composite modified electrode, *J. Food Compos. Anal.*, 2015, **40**, 14–18, DOI: 10.1016/j.jfca.2014.12.010.
13 W. Jiao, G. Ding, L. Wang, Y. Liu and T. Zhan, Polyaniline functionalized CoAl-layered double hydroxide nanosheets as a platform for the electrochemical detection of carbaryl and isoprocarb, *Microchim. Acta*, 2022, **189**(2), 78, DOI: 10.1007/s00604-022-05183-y.
14 P. N. Minh, H. V. Tuan, N. X. Dinh, O. V. Hoang, N. V. Cuong, D. T. B. Hop, T. Q. Tuan, N. T. Khi, T. Q. Huy and L. A. Tuan, Reduced graphene oxide-wrapped silver nanoparticles for applications in ultrasensitive colorimetric detection of Cr(VI) ions and the carbaryl pesticide, *New J. Chem.*, 2020, **44**, 7611–7620, DOI: 10.1039/D0NJ00947D.
15 R. Jemai, *et al.*, Activated porous carbon supported Pd and ZnO nanocatalysts for trace sensing of carbaryl pesticide in water and food products, *New J. Chem.*, 2022, **46**(29), 13880–13895.
16 T. H. V. Kumar, S. K. Raman Pillai, M. B. Chan-Park and A. K. Sundramoorthy, Highly selective detection of an organophosphorus pesticide, methyl parathion, using Ag–ZnO–SWCNT based field-effect transistors, *J. Mater. Chem. C*, 2020, **8**(26), 8864–8875, DOI: 10.1039/C9TC07043E.
17 J. Yoon, D. Lee, E. Lee, Y. S. Yoon and D.-J. Kim, Ag/ZnO Catalysts with Different ZnO Nanostructures for Non-enzymatic Detection of Urea, *Electroanalysis*, Jan. 2019, **31**(1), 17–21, DOI: 10.1002/elan.201800595.
18 A. Zno, M. M. Rahman, H. B. Balkhoyor and A. M. Asiri, Removal of a melamine contaminant with Ag-doped ZnO nanocomposite materials, *New J. Chem.*, 2019, 18848–18859, DOI: 10.1039/c9nj04638k.
19 M. T. Noman, N. Amor and M. Petru, Synthesis and applications of ZnO nanostructures (ZONSs): a review, *Crit. Rev. Solid State Mater. Sci.*, 2021, 1–43, DOI: 10.1080/10408436.2021.1886041.
20 K. M. Lee, C. W. Lai, K. S. Ngai and J. C. Juan, Recent developments of zinc oxide based photocatalyst in water treatment technology: a review, *Water Res.*, 2015, **88**, 428–448, DOI: 10.1016/j.watres.2015.09.045.
21 M. Nie, *et al.*, Study on electrocatalytic property of ZnO and Ag/ZnO, *Mater. Lett.*, 2020, **271**, 1277851–1277854, DOI: 10.1016/j.matlet.2020.127785.
22 G. R. S. Andrade, *et al.*, ZnO/Au nanocatalysts for enhanced decolorization of an azo dye under solar, UV-A and dark conditions, *J. Alloys Compd.*, 2017, **710**, 557–566, DOI: 10.1016/j.jallcom.2017.03.295.
23 W. He, Unraveling the Enhanced Photocatalytic Activity and Phototoxicity of ZnO/Metal Hybrid Nanostructures from Generation of Reactive Oxygen Species and Charge Carriers, *ACS Appl. Mater. Interfaces*, 2014, **6**(17), 15527–15535.
24 M. Zare, K. Namratha, S. Ilyas, A. Hezam, S. Mathur and K. Byrappa, Smart Fortified PHBV-CS Biopolymer with ZnO–Ag Nanocomposites for Enhanced Shelf Life of Food Packaging, *ACS Appl. Mater. Interfaces*, 2019, **11**(51), 48309–48320, DOI: 10.1021/acsami.9b15724.
25 L. Sun, R. Shao, L. Tang and Z. Chen, Synthesis of Ag/ZnO Nanocomposite with Excellent Photocatalytic Performance

Via a Facile Sol–Gel Method, *Adv. Mater. Res.*, 2014, **877**, 251–256, DOI: 10.4028/www.scientific.net/AMR.875-877.251.

26 B. Divband, M. Khatamian, G. R. K. Eslamian and M. Darbandi, Applied Surface Science Synthesis of Ag/ZnO nanostructures by different methods and investigation of their photocatalytic efficiency for 4-nitrophenol degradation, *Appl. Surf. Sci.*, 2013, **284**, 80–86, DOI: 10.1016/j.apsusc.2013.07.015.

27 D. Y. Nadargi, M. S. Tamboli, S. S. Patil, I. S. Mulla and S. S. Suryavanshi, Development of Ag/ZnO nanorods and nanoplates at low hydrothermal temperature and time for acetone sensing application : an insight into spillover mechanism, *SN Appl. Sci.*, 2019, **1**, 1564, DOI: 10.1007/s42452-019-1573-2.

28 Y. Wei, *et al.*, Materials Science in Semiconductor Processing Hydrothermal synthesis of Ag modi fi ed ZnO nanorods and their enhanced ethanol-sensing properties, *Mater. Sci. Semicond. Process.*, 2017, 1–7, DOI: 10.1016/j.mssp.2017.11.007.

29 E. Mendoza-Mendoza, *et al.*, One-step synthesis of ZnO and Ag/ZnO heterostructures and their photocatalytic activity, *Ceram. Int.*, 2018, **44**, 6176–6180, DOI: 10.1016/j.ceramint.2018.01.001.

30 X. Zhai, *et al.*, Analytica Chimica Acta A highly selective and recyclable sensor for the electroanalysis of phosphothioate pesticides using silver-doped ZnO nanorods arrays, *Anal. Chim. Acta*, 2021, **1152**, 338285, DOI: 10.1016/j.aca.2021.338285.

31 N. Sebastian, *et al.*, Ultrasensitive Electrochemical Detection and Plasmon-Enhanced Photocatalytic Degradation of Rhodamine B Based on Dual-Functional, 3D, Hierarchical Ag/ZnO Nanoflowers, *Sensors*, 2022, **22**(13), 5049, DOI: 10.3390/s22135049.

32 B. Y. Sahyar, M. Kaplan, M. Ozsoz, E. Celik and S. Otles, *Bioelectrochemistry*, 2019, 107327, DOI: 10.1016/j.bioelechem.2019.107327.

33 H. D. Kiriarachchi, K. M. Abouzeid, L. Bo and M. S. El-Shall, Growth Mechanism of Sea Urchin ZnO Nanostructures in Aqueous Solutions and Their Photocatalytic Activity for the Degradation of Organic Dyes, *ACS Omega*, 2019, **4**(9), 14013–14020, DOI: 10.1021/acsomega.9b01772.

34 S. Kwon, D. Kim, S. Jung and Y. Hwu, Microwave synthesis of gold nanoparticles : Effect of applied microwave power and solution pH, *Mater. Chem. Phys.*, 2011, **131**(1–2), 331–335, DOI: 10.1016/j.matchemphys.2011.09.050.

35 Z. Zou, *et al.*, Opposite Particle Size Effect on Amorphous Calcium Carbonate Crystallization in Water and during Heating in Air, *Chem. Mater.*, 2015, **27**(12), 4237–4246, DOI: 10.1021/acs.chemmater.5b00145.

36 G. P. Barreto, G. Morales and M. L. L. Quintanilla, Microwave Assisted Synthesis of ZnO Nanoparticles: Effect of Precursor Reagents, Temperature, Irradiation Time, and Additives on Nano-ZnO Morphology Development, *J. Mater.*, 2013, **2013**(1), 1–11, DOI: 10.1155/2013/478681.

37 N. T. Anh, *et al.*, PAPER electrochemical nanosensors for the detection of furazolidone in pork and shrimp samples : exploring the role of crystallinity , phase ratio , and, *New J. Chem.*, 2022, **46**, 7090–7102, DOI: 10.1039/D1NJ05837A.

38 G. Kesavan, M. Pichumani and S. Chen, Influence of Crystalline, Structural, and Electrochemical Properties of Iron Vanadate Nanostructures on Flutamide Detection, *ACS Appl. Nano Mater.*, 2021, **4**(6), 5883–5894, DOI: 10.1021/acsanm.1c00802.

39 A. de la Escosura-Muñiz, C. Parolo, F. Maran and A. Mekoçi, Size-dependent direct electrochemical detection of gold nanoparticles: application in magnetoimmunoassays, *Nanoscale*, 2011, **3**(8), 3350, DOI: 10.1039/c1nr10377f.

40 A. Sangili, V. Vinothkumar, S. Chen, P. Veerakumar and K. Lin, Gold Nanoparticle Embedded on a Reduced Graphene Oxide/polypyrrole Nanocomposite: Voltammetric Sensing of Furazolidone and Flutamide, *Langmuir*, 2020, **36**(46), 13949–13962, DOI: 10.1021/acs.langmuir.0c02448.

41 M. Saqib, E. V. Dorozhko, J. Barek, V. Vyskocil, E. I. Korotkova and A. V. Shabalina, A Laser Reduced Graphene Oxide Grid Electrode for the Voltammetric Determination of Carbaryl, *Molecules*, 2021, **26**(16), 5050, DOI: 10.3390/molecules26165050.

42 T. N. Pham, *et al.*, Insight into the Influence of Analyte Molecular Structure Targeted on MoS2-GO-Coated Electrochemical Nanosensors, *Langmuir*, 2021, **37**(41), 12059–12070, DOI: 10.1021/acs.langmuir.1c01853.

43 H. Zhai, Z. Liu, Z. Chen, Z. Liang, Z. Su and S. Wang, A sensitive electrochemical sensor with sulfonated graphene sheets/oxygen-functionalized multi-walled carbon nanotubes modified electrode for the detection of clenbuterol, *Sens. Actuators, B*, 2015, **210**, 483–490, DOI: 10.1016/j.snb.2014.12.121.

44 E. Laviron, General expression of the linear potential sweep voltammogram in the case of diffusion less electrochemical systems, *J. Electroanal. Chem. Interfacial Electrochem.*, 1979, **101**, 19–28.

45 T. Yin, *et al.*, The catalytic effect of TiO_2 nanosheets on extracellular electron transfer of Shewanella loihica PV-4, *Phys. Chem. Chem. Phys.*, 2016, **18**, 29871–29878, DOI: 10.1039/C6CP04509J.

46 P. Hashemi, N. Karimian, H. Khoshsafar, F. Arduini and M. Mesri, Materials Science & Engineering C Reduced graphene oxide decorated on Cu/CuO-Ag nanocomposite as a high- performance material for the construction of a non-enzymatic sensor : Application to the determination of carbaryl and fenamiphos pesticides, *Mater. Sci. Eng., C*, 2019, **102**, 764–772, DOI: 10.1016/j.msec.2019.05.010.

47 N. Le *et al.*, Bio-AgNPs-based electrochemical nanosensors for the sensitive determination of 4-nitrophenol in in physicochemical parameters and sensing," pp. 6007–6017, 2022, DOI: 10.1039/d1ra09202b.

48 D. B. Priya and I. V. Asharani, Size Dependent Catalytic Activity of Actinodaphne madraspatana Bedd Leaves Mediated Silver Redox potential sil, *J. Cluster Sci.*, 2017, **28**, 1837–1856, DOI: 10.1007/s10876-017-1185-1.

49 M. Zhang, Z. Zhang, Y. Yang, Y. Zhang, Y. Wang and X. Chen, Ratiometric Strategy for Electrochemical Sensing of Carbaryl Residue in Water and Vegetable Samples, *Sensors*, 2020, **20**(5), 1524, DOI: 10.3390/s20051524.

50 F. C. Moraes, L. H. Mascaro, S. A. S. Machado and C. M. A. Brett, Direct electrochemical determination of carbaryl using a multi-walled carbon nanotube/cobalt phthalocyanine modified electrode, *Talanta*, 2009, **79**, 1406–1411, DOI: 10.1016/j.talanta.2009.06.013.